Materials Science & Engineering A 831 (2022) 142094

Contents lists available at ScienceDirect

Materials Science & Engineering A

journal homepage: www.elsevier.com/locate/msea

Microstructure evolution and fracture mechanism of a TiAl–Nb alloy during high-temperature tensile testing

Shunke Zhang [a,b], Ning Tian [a,b,*], Deyuan Li [a,**], Jianghua Li [c], Fangwei Jin [b], Guangyan Wang [b], Sugui Tian [a,b]

[a] Shenyang University of Technology, Shenyang, 110870, China
[b] Guizhou University of Engineering Science, Bijie, 551700, China
[c] State Key Laboratory of Nonlinear Mechanics (LNM), Institute of Mechanics, Chinese Academy of Sciences, Beijing, 100190, China

ARTICLE INFO

Keywords:
TiAl-Nb alloy
Microstructure
Deformation mechanism
Damage features

ABSTRACT

A TiAl–Nb alloy was prepared by casting, and its tensile properties and microstructure evolution at different temperatures were investigated. The results show that the brittle-ductile transition temperature (BDTT) of the alloy is 880–920 °C. At low temperatures, deformation mainly occurs in the γ lamellae and coarsening γ phase between the lamellar colonies. As the temperature increase in the transitory stage, a small number of dislocations may pass through the interface from the coarsening γ phase into the γ lamellae. During the brittle stage, the dislocation and dislocation array bow out from the phase interface, and twins are emitted from the phase interface, which may contribute to the accommodation of stress concentration. During the ductile stage, the γ lamellae coarsen due to the thinner and smaller α_2 lamellae dissolving and phase boundary transfer. The dislocations interact with the dislocation walls to form subboundaries in the γ lamellae and transform into equiaxed crystals by dynamic recrystallization (DRX), which increases the plasticity of the alloy. With the transition from the brittle model to the ductile model, the fracture mode of the alloy changes from the mixed fracture mode of transgranular fracture and translaminar fracture to intergranular fracture.

1. Introduction

With the development of the aerospace industry, the properties of high-temperature structural materials are increasingly demanding. Compared to Ni-based alloys, TiAl alloys have a higher specific strength, higher specific stiffness, and lower density. They are expected to replace nickel-based superalloys and become high-temperature structural materials with great potential in the aerospace industry [1]. Therefore, an increasing number of researchers are studying the high-temperature properties of TiAl alloys.

The high-temperature properties of TiAl alloys are associated with the lamellar spacing, colony size and boundary structures [2]. Leitner [3] created four different alloys with different grain sizes, volume fractions, and boundary structures and found that the fracture mechanism was most dependent on the structure and phase arrangement at the boundaries. Voisin [4] performed tensile tests on the Ti–48Al–2W-0.08 B alloy and found ordinary dislocations and twins activated in the γ grains and γ lamellae. In addition, dislocations were emitted at an α_2/γ lamellar interface and propagated across the lamellae, as observed by in situ TEM.

Zhao [5] investigated the microstructure and tensile properties after isothermal and cyclic high-temperature exposures. They found that the destruction of lamellar interfaces, fracture of α_2 phases and coalescence of neighbouring γ lamellae induced the coarsening of lamellar structures and deteriorated the tensile properties of the γ-TiAl alloy. Imayev [6] concluded that the main reason for the brittle-ductile transition was thermal activation, the brittle stage, which was controlled by the relaxation of grain boundaries, and the ductile stage, which was controlled by the relaxation of the grain interior. Wang [7] proposed that the creep strain and creep life significantly changed during creep at the brittle-ductile transition temperature because the dislocation slip systems of α_2 lamellae were activated above the brittle-ductile transition temperature. Many studies indicate that the brittle-ductile transition is closely related to the texture evolution, mechanical twins, dislocation

* Corresponding author. Guizhou University of Engineering Science, Bijie, 551700, China
** Corresponding author.
E-mail addresses: syhgxytn@163.com (N. Tian), dmy1962@sina.com (D. Li).

https://doi.org/10.1016/j.msea.2021.142094
Received 19 January 2021; Received in revised form 12 August 2021; Accepted 17 September 2021
Available online 22 September 2021
0921-5093/© 2021 Elsevier B.V. All rights reserved.

slip, deformation bands and dynamic recrystallization [8–16].

In this paper, a high-performance Nb–TiAl alloy was designed by adjusting the alloying composition and microstructure to provide a theoretical basis for its optimization for engineering applications.

2. Experimental materials and methods

The TiAl–Nb master alloy with a nominal composition of Ti–44Al–8Nb-0.2W-0.2B-0.1Y (at. %) was fabricated into an ingot using a vacuum induction skull melting furnace; refer to Ref. [17] for a detailed experimental procedure. The composition determined by X-ray fluorescence spectroscopy is listed in Table 1. Then, the alloy ingot was processed into an I-shaped flake sample with a cross-section of 4.5 mm and a standard distance of 20 mm by wire cutting.

After being ground and polished, the samples were tested by a WDW-100 high-temperature electronic tensile testing machine. The sample was clamped to a special fixture, and the sample was placed in the center of a resistance furnace. Then, the temperature was raised to the corresponding temperature and tested at a rate of 1×10^{-3}/s. The resistance furnace used a three-stage temperature control, and the temperature fluctuation was less than 2 °C. The microstructure and morphology of the as-cast samples before and after tensile fracture under different conditions were observed using scanning electron microscopy (SEM), transmission electron microscope (TEM), electron backscattered diffraction (EBSD) and High-resolution transmission electron microscope (HRTEM) to study the deformation and damage characteristics of the alloy during the tensile test.

3. Experimental results and analysis

3.1. Microstructure of the alloy

The microstructure of the alloy in the cast state is shown in Fig. 1. Fig. 1(a) shows an SEM image of the specimen in the cast state. The microstructure of the alloy was composed of lamellar colonies and serrated colony boundaries. Fig. 1(b) and (c) show the image quality map and phase map of the TiAl–Nb alloy. It can be seen that the alloy consists of approximately 88.6% γ and 11% α_2. The lamellar colony boundaries was composed of coarsening γ phase, as shown by the dotted lines in Fig. 1(c) and white arrows in Fig. 1(a). A few β(B2) phases were located at the surface between the lamellar colony and coarsening γ phase. Fig. 1(d) shows a TEM image of the specimen in the cast state. According to the selected diffraction pattern (SDP), the microstructure of the lamellar colony was composed of the γ-TiAl phase and α_2-Ti_3Al phase, sharing a common interface plane. A small number of dislocations exist in the γ lamellae, and the width of the γ lamellae is much larger than that of the α_2 lamellae.

3.2. Tensile properties of the alloy

The tensile curves for the TiAl–Nb alloy at 800 °C–920 °C are shown in Fig. 2(a). It can be seen that the stress increases sharply with the increase of elongation, and the curves break off in the hardening stage at lower temperature (800–840 °C). At 900 °C and 920 °C, the curves with a peak and then decrease, the strength decrease as the temperature increase.

The yield strength and elongation of the materials were compared at different temperatures, as shown in Fig. 2(b). The yield strength and elongation changed slightly in the range of 800–880 °C (the elongation refers to the fracture strain, and the yield strength refers to the fracture strength). At 920 °C, the yield strength sharply decreased and the elongation sharply increased (the elongation refers to fracture strain, and the yield strength refers to 0.2% plastic strain). Then the brittle-ductile transition temperature (BDTT) of the material was 880–920 °C, and 900 °C was the transitory stage between the brittle temperature and ductile temperature.

Table 1
Composition of the sample, as measured by X-ray fluorescence spectroscopy.

Element	Al	Y	Nb	Ti	W	other
Atomic %	47.19	0.18	8.26	42.17	0.36	**
Error %	3.21	**	0.82	1.66	**	**

3.3. Phase transition during high-temperature tensile processes

Fig. 3 shows the EBSD observation results of the as-cast TiAl–Nb alloy. Fig. 3(a) and (b) are the image quality map and corresponding phase map, respectively. They indicate that the alloy consists of approximately 91.5% γ, 8.4% α_2, and a few β(B2) phases, i.e., there is much more γ phase than α_2 phase. Fig. 3(c) shows the grain boundary map (the grain boundary here is actually the phase boundary). Only high-angle grain boundaries (HAGBs), grain boundaries whose adjacent grains exhibit an orientation difference greater than 15°, are present. Moreover, the comparison of Fig. 3(c) with Fig. 3(b) shows that the α_2 phase is characterized by lamellae and that the boundaries are straight. Fig. 3(d) shows the kernel average misorientation (KAM) map, which can be used to assess the local misorientation, where a higher local misorientation reflects a higher dislocation density. This result indicated that there were a small number of local dislocations in the alloy. Fig. 3(e) shows the inverse pore figure (IPF) map. Interestingly, γ lamellae have three orientations, lamellae γ_1, γ_2 and γ_3, in Fig. 3(e), while α_2 lamellae have only one orientation with euler angles of approximately 282.0, 99.4, and 106.7°.

The pole figures of the four phases (γ_1, γ_2, γ_3 and α_2), as marked by arrows in Fig. 3(e), are shown in Fig. 4. Fig. 4(a) and (e) shows the {0001} and {11–20} pole figures of the α_2 phas e. Fig. 4(b), (c) and (d) shows the {111}, {101} and {110} pole figures of the γ_1 phase. Fig. 4(f), (g) and (h) shows the {111}, {101} and {110} pole figures of the γ_2 phase. Fig. 4(i), (g) and (k) shows the {111}, {101} and {110} pole figures of the γ_3 phase. The focus of the pole shows one of the projection planes. For example, the four focus poles in Fig. 4(b) are the projections of four (111) planes of γ1. The focus of the pole coincidence indicates that the corresponding crystal planes are parallel [18].

According to Fig. 4(a), (b), (f) and (i), the orientation relationship of α_2, γ_1, γ_2 and γ_3 is identified as $\{0001\}_{\alpha2}//\{111\}_{\gamma1}//\{111\}_{\gamma2}//\{111\}_{\gamma3}$. Analogously, according to Fig. 4(c), (d), (e), (g), (h), (j) and (k), the orientation relationship of α_2, γ_1 and γ_2 is $\{11–20\}_{\alpha2}//\{101\}_{\gamma1}//\{110\}_{\gamma1}//\{101\}_{\gamma2}\{110\}_{\gamma2}\{101\}_{\gamma3}//\{110\}_{\gamma3}$.

Fig. 5 shows the EBSD observation results of the TiAl–Nb specimen after tensile fracture at 920 °C. Fig. 5(a) and (b) show the image quality map and corresponding phase map, respectively. Compared to the as-cast state alloy (Fig. 3(b)), the area fractions of the γ phase, α_2 phase and β(B2) phase were almost unchanged. Comparing Fig. 5(a)–(b) with Fig. 3(a)-(b), some γ/γ interfaces disappeared, and some broken α_2 lamellae dissolved, which may be the result of coarsening the γ lamellae [19]. In addition, coarsening and bending of α_2 lamellae were observed, as marked by the black dotted lines in Fig. 5(b). The fraction of low-angle grain boundaries increased from 0 (Fig. 3(c)) to 34.2% (Fig. 5(c)), and more low-angle grain boundaries (LAGBs) and high-angle grain boundaries (HAGBs) appeared in the γ lamellae due to dynamic recovery (DRV) and DRX, as shown by the red dotted lines in Fig. 5(c). Fig. 5(d) shows the KAM map, indicating that the local strain in the γ lamellar region undergoing DRV and DRX is heavily concentrated. Fig. 5(e) shows that the γ lamellae presents four orientations, while the α_2 lamellae still has only one orientation with Euler angles of approximately 262.1°, 149.1°, and 279.4°. From the above pole figure analysis method, their orientation relationships are determined as follows: $(0001)_{\alpha2}//(111)_{\gamma1\sim\gamma4}$, $(11–20)_{\alpha2}//(101)_{\gamma1\sim\gamma4}$, $(101)_{\gamma1}//(101)_{\gamma2}//(110)_{\gamma3}//(110)_{\gamma4}$, $(110)_{\gamma2}//(101)_{\gamma3}//(101)_{\gamma4}$ and $(110)_{\gamma3}//(110)_{\gamma4}$.

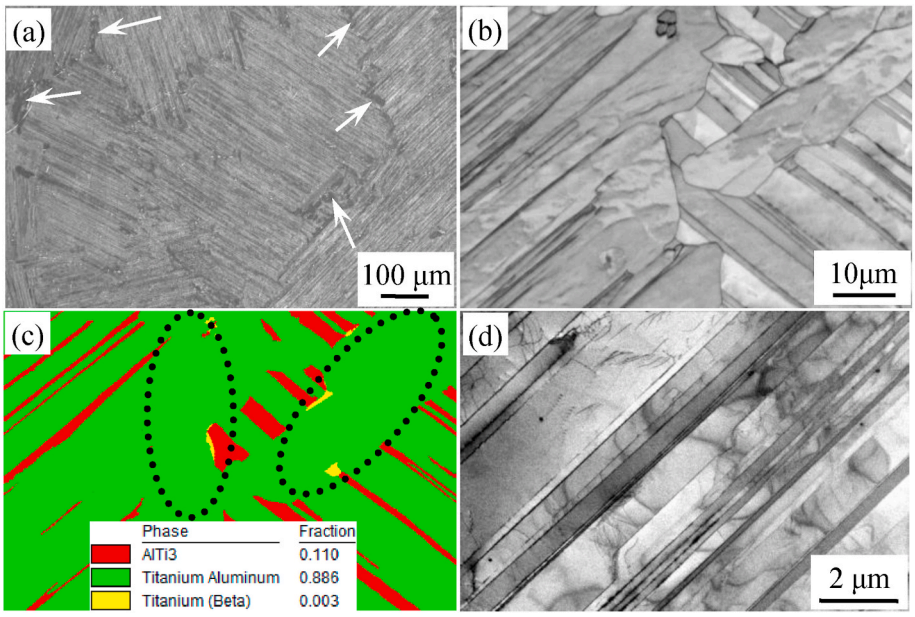

Fig. 1. Microstructure of the TiAl–Nb alloy: (a) SEM image; (b) TEM image; (c) electron image; and (d) phase map.

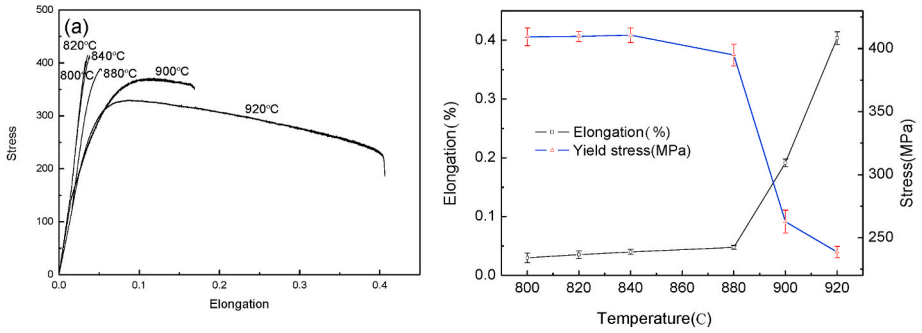

Fig. 2. Relationship between tensile properties and temperature: (a) stress as a function of elongation and (b) stress as a function of temperature.

3.4. Deformation characteristics of the alloy during the brittle stage

The microstructure between the lamellar colony and coarsening γ phase after tensile fracture in the brittle stage is shown in Fig. 6. Fig. 6(a) shows the bright field TEM images near the fracture after tensile fracture at 800 °C. Fig. 6(b) shows the EDS maps of Ti for the region in Fig. 6(a). In the EDS maps, the bright contrast region with higher Ti content is the α_2 phase, and the dark contrast region is the γ phase. The diffraction pattern in Fig. 6(c) shows the same result. There were few dislocations in the γ lamellae and more dislocations in the coarsening γ phase, and the dislocations were blocked by the interface between the lamellar colony and coarsening γ phase, as shown by the white circles in Fig. 6(a). The enlarged view in the white circles is shown in Fig. 6(c).

Fig. 7(a) is the bright field TEM image of the lamellar colony region near the fracture after tensile fracture at 820 °C, where the bright contrast region is the γ phase, and the dark contrast region is the α_2 phase. Many twins were emitted from the γ/α_2 lamellar interface, travelled a short distance in the γ lamellae and ended at the γ/α_2 phase boundary. Most of the twins were at an angle of nearly 90° from the γ/α_2 phase boundary, while a small number of twins were at a smaller angle from the γ/α_2 phase boundary. There are also dislocation arrays in the γ lamellae. After the dislocation array passed through the twins, the dislocation spacing of the dislocation arrays increased, as shown by the black arrows in Fig. 7(a). Thus, the twins had a small blocking effect on the dislocation array, and the dislocation array continued to move through the twins. No significant dislocations or twins were found in the α_2 lamellae. Fig. 7(b) shows another region after tensile fracture at 820 °C. The γ/γ phase boundaries (high-angle boundaries) absorbed the lattice dislocations. As mentioned in Ref. [20], the boundary of the alloy was observed in the TEM image as a ribbon with parallel sides. Lattice dislocations entered the phase boundary, as shown by the white arrow, and the enlarged view is shown in the lower left corner of the figure. Lattice dislocations trapped by phase boundaries are shown by the black arrow, and the enlarged view is shown in the upper right corner of the figure; a similar result was observed in other metals [6].

The microstructure deformation of the alloy after tensile fracture at 840 °C is shown in Fig. 7(c). The deformation of the lamellar colony mainly remained in the γ lamellae. The twins were emitted from the γ/α_2 lamellar interface, and the dislocations bowed out from the γ/α_2 lamellar interface in the same place, as shown by the white arrows in the figure. Moreover, many laminations were found inside the twins, as shown by the black arrows in the figure. Another region of this specimen is shown in Fig. 7(d), where dislocations and dislocation arrays were emitted from the γ/α_2 interfaces.

Fig. 8(a) shows the microstructure of the alloy after tensile fracture at 880 °C; the SAD of the area in the rectangular wire frame, which is marked A, is shown in Fig. 8(b), and the SDP of the area in the triangle wire frame, which is marked B, is shown in Fig. 8(c). The thin lath in the rectangular wire frame and phase interface comprised twins. Fig. 8(d) shows an HRTEM image of the circular wire frame marked C in Fig. 8(a).

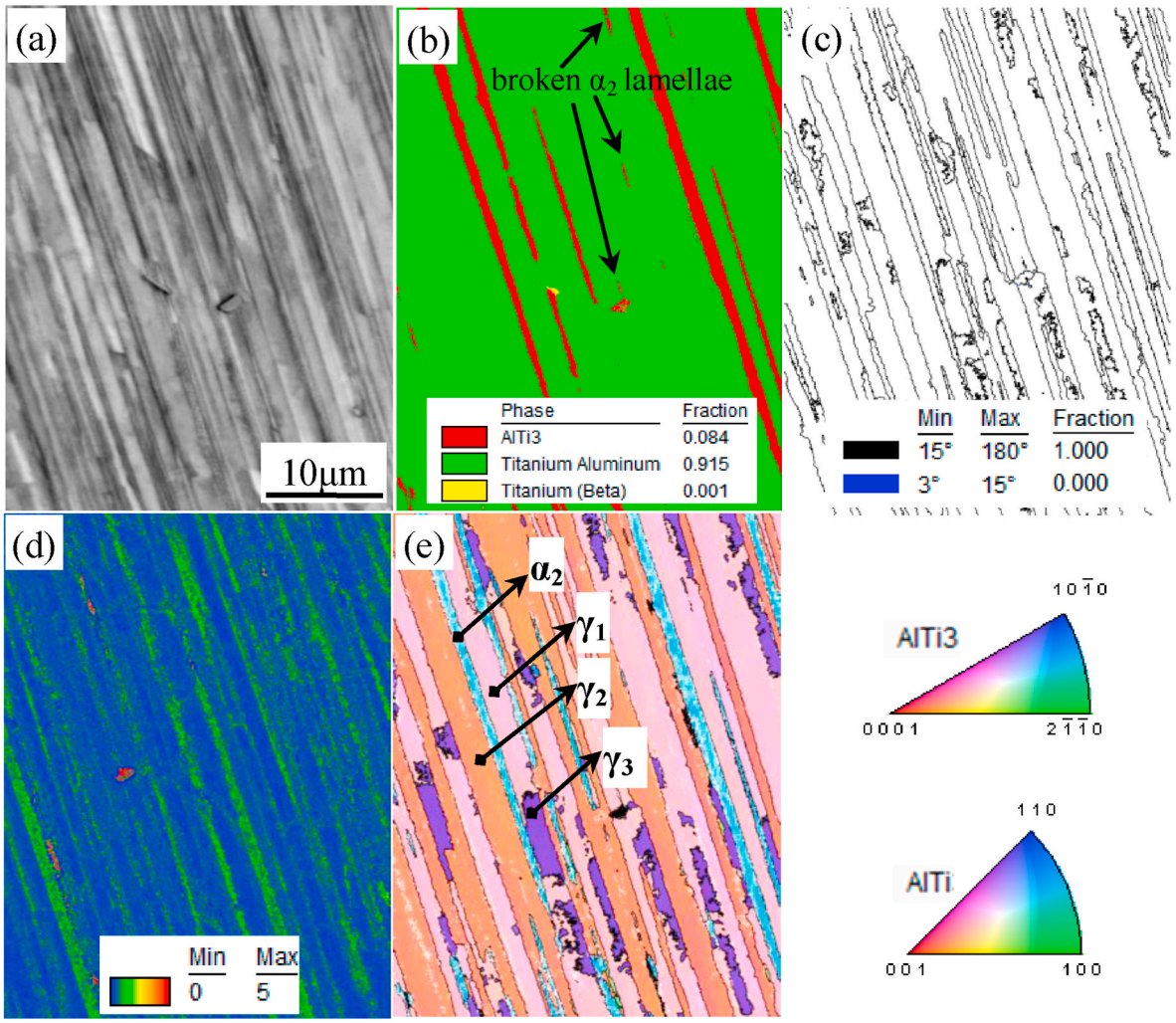

Fig. 3. EBSD observation results of the as-cast alloy: (a) image quality map; (b) phase map; (c) grain boundary map; (d) KAM map; and (e) IPF.

This result indicates that twin nucleation occurs at the misfit dislocations of γ/γ interfaces, as shown in the rectangular wire frame. This phenomenon was also observed at other temperatures (820 °C–880 °C).

3.5. Deformation characteristics of the alloy during the transitory stage

The bright field TEM images after tensile fracture at 900 °C are shown in Fig. 9. Fig. 9(b) shows the EDS map of Al in the area in Fig. 9 (a). Many dislocations were present in the coarsening γ phase and γ lamellae and remained blocked by the interface, as shown by the area in the white circles in Fig. 9(a), whose enlarged view is shown in Fig. 9(c). However, there is another region in Fig. 9(d): high-density dislocations and many dislocation tangles were produced in the coarsening γ phase and γ lamellae. Fig. 9(e) and (f) show the enlarged view of regions A and B (in the white circle wireframe) in Fig. 9(d). Few dislocations may pass through the interface from the coarsening γ phase into the γ lamellae.

3.6. Deformation characteristics of the alloy during the ductile stage

Fig. 10(a)-10(e) show the microstructure deformation of the alloy after tensile fracture at 920 °C. As shown in Fig. 10(a), the dislocation in the γ lamellae perpendicular to the γ/α_2 interface fastens to the γ/α_2 interface. The dislocation in the γ lamellae perpendicular to the γ/α_2 interface reacts with the dislocation parallel to the γ/α_2 interface to form a dislocation network, as shown by the black arrow; the enlarged view is shown in the lower left corner of the figure. In addition, γ phase coarsening can be observed obviously. Fig. 10(b) shows another region after tensile fracture at 920 °C; the dislocations continued to move primarily in the γ lamellae, and the dislocation density sharply increased. With an increase in temperature, the actuated slip system increased, the dislocation line was curved, dislocation interactions occurred, and dislocation jogs formed, which indicates that the dislocations underwent cross-slip and climb during the deformation process [21]. The dislocations in the γ lamellae entangled near the phase boundary to form dislocation walls parallel to the interface, as shown in the enclosed area in the white rectangular wireframe in Fig. 10(b), and few dislocations were found in the α_2 phase region, as shown by the white arrows in Fig. 10(b); the enlarged view is shown in the lower left corner of the figure. Many dislocations accumulated in the lamellae to form dislocation walls. When reaching the dislocation wall, the moving free dislocations interact with the wall dislocations. This interaction results in more regular and stable dislocation subboundaries that separate the subgrain regions of the crystal with a relatively low dislocation density. The subboundaries are shown by white arrows in Fig. 10(c). When plastic deformation occurs at higher temperatures, the cross-slip of dislocations is assisted by diffusion processes. Thus, the annihilation of dislocations of the opposite sign is much easier, which also reduces the dislocation density. The α_2 phase dissolved during high-temperature deformation, as shown by the white arrows in Fig. 10(d). The phase boundary and dislocation arrays remained where the α_2 phase dissolved, as shown by the black arrow in Fig. 10(d). The enlarged view is shown in the upper right corner of the figure. Some boundaries remained flat,

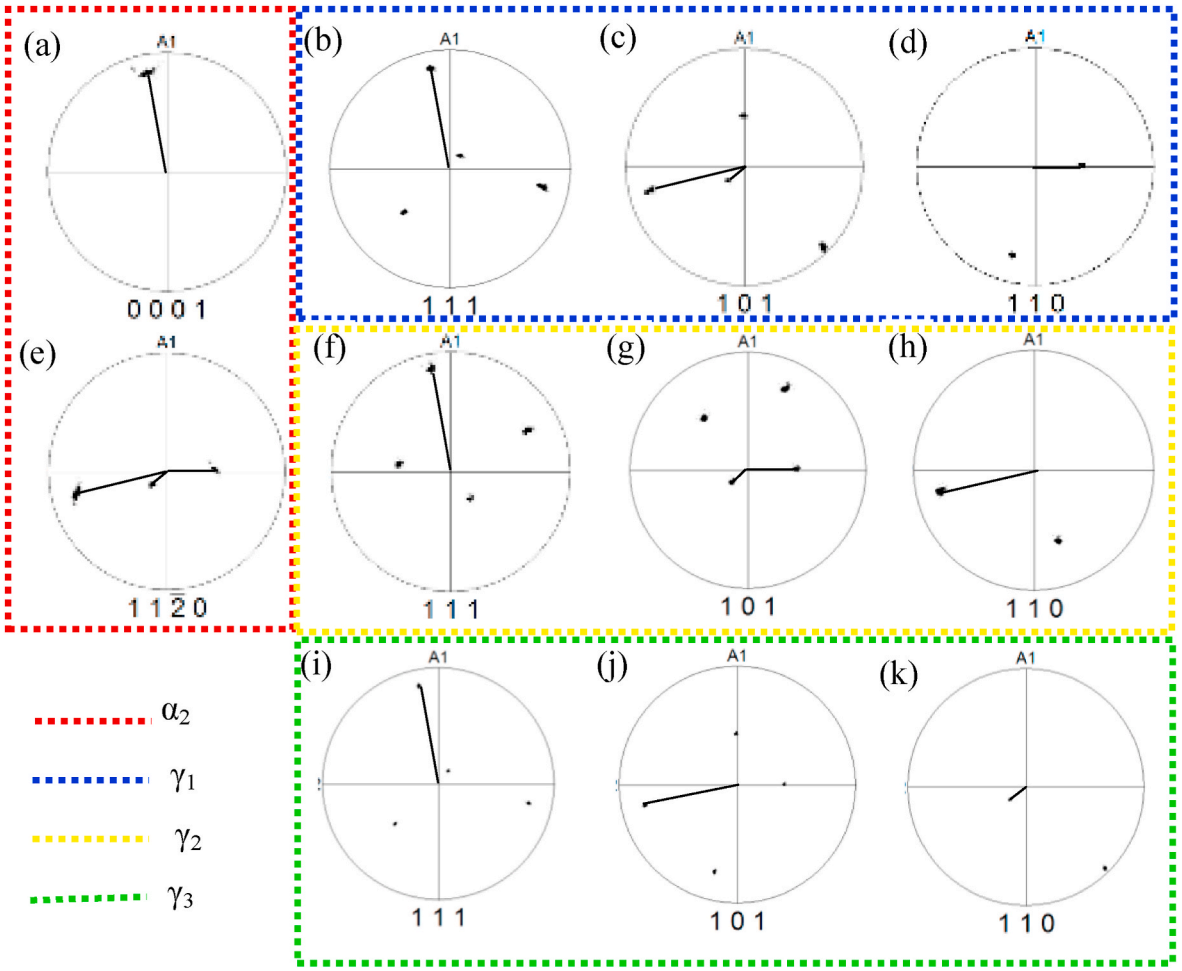

Fig. 4. Pole figures of the four phases in Fig. 3(e): (a) (e) pole figures of lamellae α_2; (b), (c) and (d) pole figures of lamellae γ_1; (f), (g) and (h) pole figures of lamellae γ_2; and (i), (j) and (k) pole figures of lamellae γ_3.

while others became curved and irregular. The subgrains produced by DRV can be clearly observed in γ lamellae, as shown in Fig. 10(e). Some of the DRV grains twisted, and DRX occurred.

3.7. Initiation and propagation of cracks

The fracture microstructure of the TiAl–Nb alloy at 820 °C is shown in Fig. 11(a)-11(b), and the direction of the applied stress is labelled by the white double-headed arrow in Fig. 11(b). During the tensile test, when the lamellar direction was almost vertical to the stress axis, cracks of different sizes were generated at the α_2/γ lamellar interface and spread along the lamellar phase boundary, as shown by the white arrows in Fig. 11(a). Fig. 11(b) is a magnified view of the local microstructure in the region in the white box in Fig. 11(a). When the orientation difference between two adjacent lamellar colonies was small, a crack could be deflected at an angle and could expand into another lamellar colony, as shown by the short white arrow in Fig. 11(b). When the orientation difference between two adjacent lamellar colonies was large, the crack expansion to the lamellar colony boundary was blocked, and the crack could expand to both ends along the lamellar colony boundary, as shown by the long white arrow in Fig. 11(b). Two cracks in different lamellar colonies could be connected to each other by tearing edges to form larger cracks, as shown by the black arrow, and the magnified view is shown in the lower left.

Fig. 11(c) shows the fracture microstructure of the TiAl–Nb alloy at 840 °C. The crack continued to expand along the lamellar interface (as shown by the black arrow) when the angle between the lamellar direction and the stress axis direction was small. However, due to the large expansion resistance along the lamellae, when the expansion resistance exceeded the strength of the lamellar colony, the crack led to several lamellar fractures through the shear lamellar structure (as shown by the white arrow). Then, it continued to expand along the lamellar interface. Finally, multiple cracks bridged into a large step-like crack, which is consistent with the observed fracture microstructure in Fig. 13 (b). The γ lamellar layer was weakened at this temperature, and cracks first appeared in the lamellae.

The fracture microstructure of the alloy at 920 °C is shown in Fig. 12 (a)-12(d). The direction of the applied stress is marked by a white double-headed arrow. Cavities could be generated in the lamellar colony boundary and lamellar colony but could not expand in the lamellar colony, as shown by the white arrows in Fig. 12(a)-12(b). At the lamellar colony boundary, the cavities interconnected to form large cracks, as shown by the black arrows. When the crack was nearly 45° from the stress axis, i.e., in the soft orientation, the crack growth resistance was small, and the crack size was small in the width direction, as shown in Fig. 12(a). When the crack was nearly perpendicular to the stress axis, i.e., the hard orientation, the crack propagation resistance was large, and the crack size was large in the width direction. Moreover, the alloy lamellar colonies experienced a large stress, and the lamellar structure was bent, as shown in Fig. 12(b).

Fig. 12(c)-12(d) show another region after tensile fracture at 920 °C. Dynamically recrystallized lamellar colonies easily occurred in the lamellar colony boundary region during high-temperature elongation, and cavities easily formed in the DRX region, as shown in Fig. 12(c). The

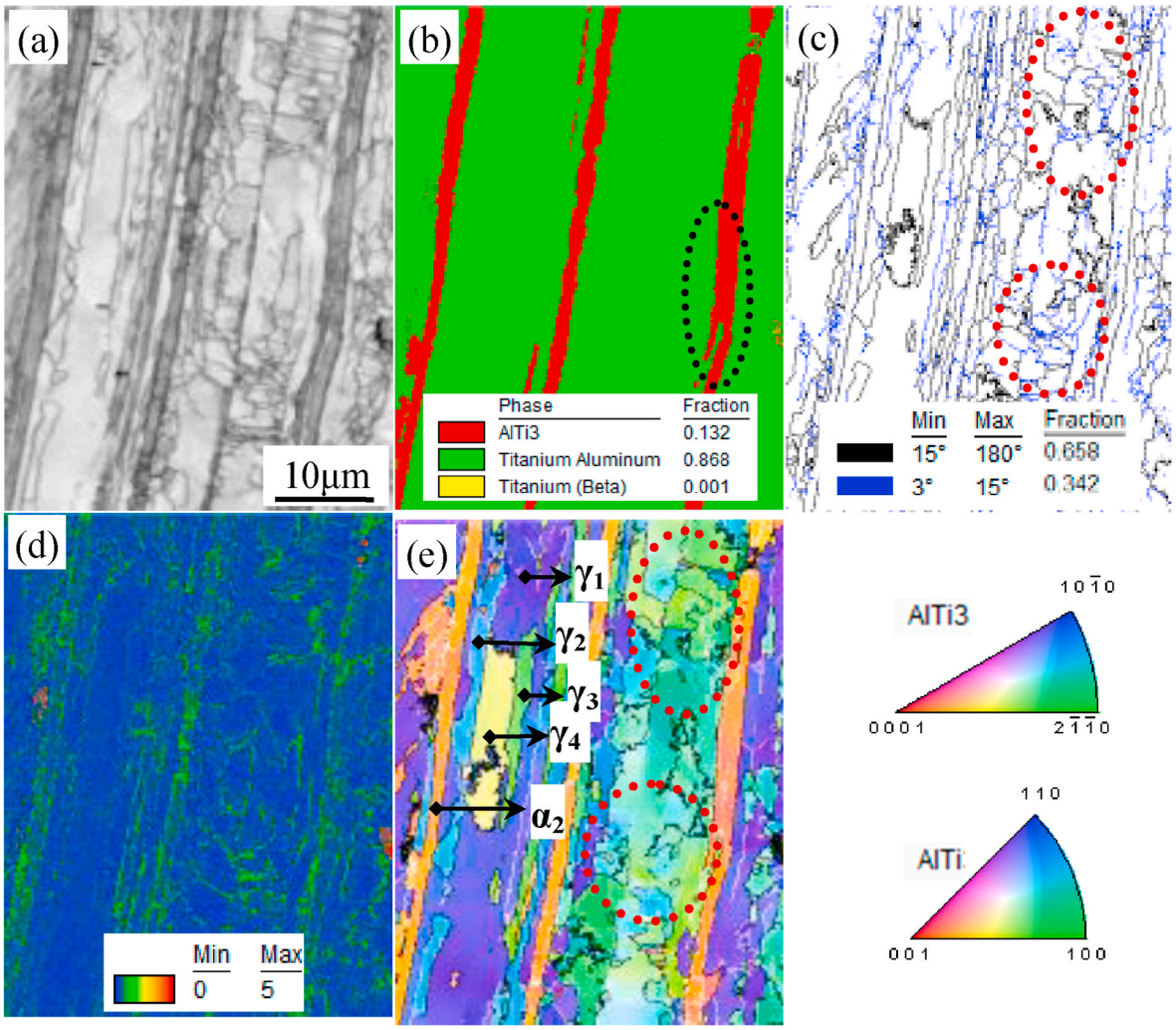

Fig. 5. EBSD observation results of the as-cast alloy near the fracture after tensile fracture at 920 °C: (a) image quality map; (b) phase map; (c) grain boundary map; (d) KAM map; and (e) IPF.

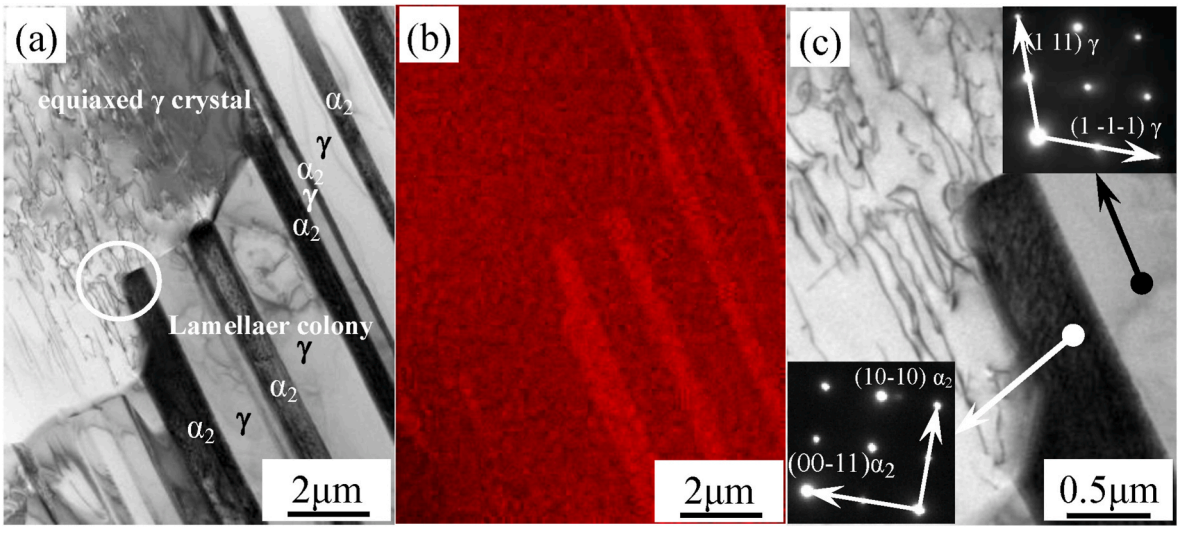

Fig. 6. Deformation features of the alloy after tensile fracture at 800 °C: (a) TEM image of the fracture microstructure; (b) EDS map of Ti; and (c) enlarged view of (a).

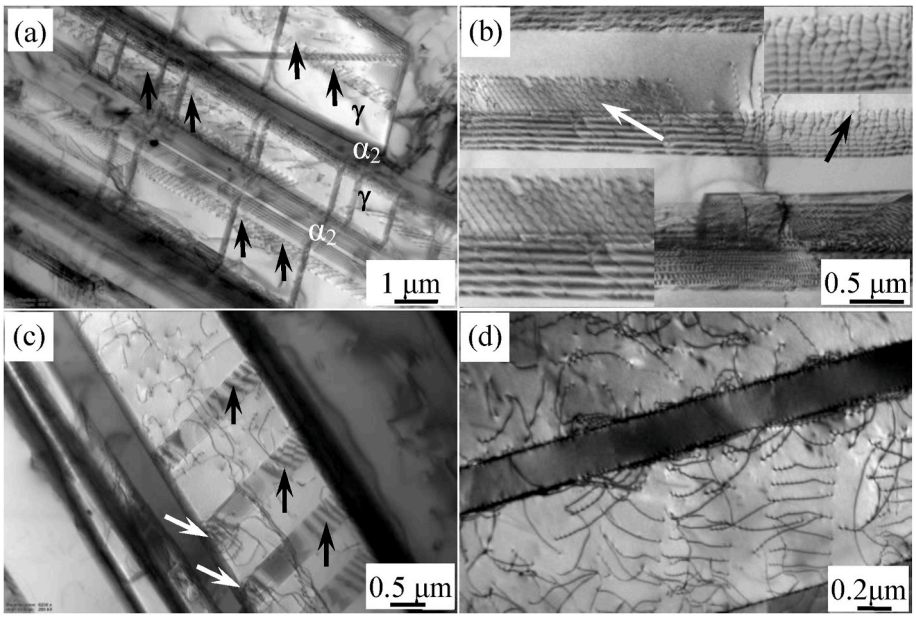

Fig. 7. Deformation features of the alloy after tensile fracture during the brittle stage: (a)–(b) 820 °C and (c)–(d) 840 °C.

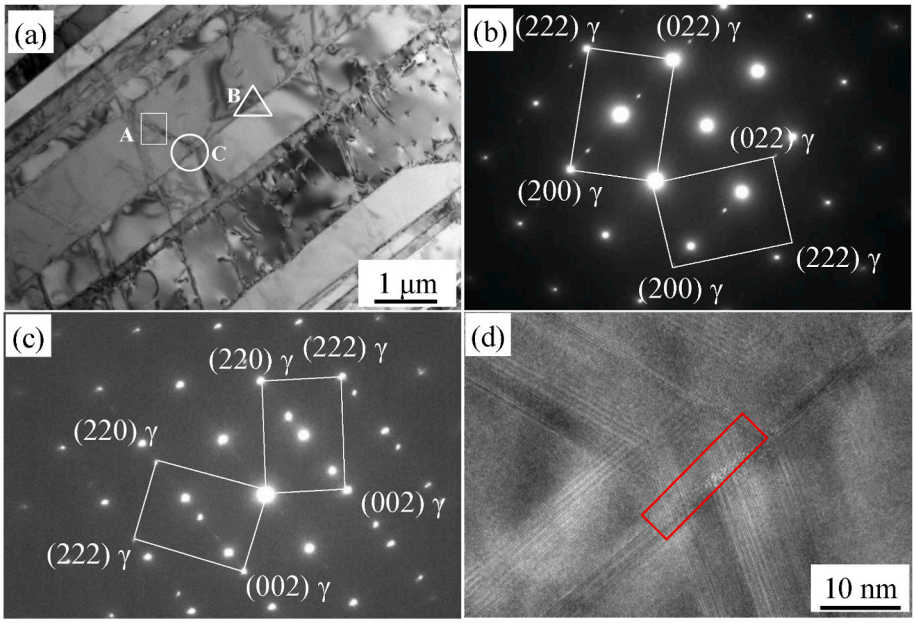

Fig. 8. Deformation features in the alloy after tensile fracture at 880 °C. (a) TEM image of the alloy; (b) SDP of area A; (c) SDP of area B; and (d) HRTEM image of area A.

cavities interconnected to form large cracks, as shown in Fig. 12(d). In addition, the lamellar structure was bent.

The microstructure after tensile fracture at different temperatures is shown in Fig. 13. Fig. 13(a) shows the fracture microstructure of the alloy at 800 °C. The alloy exhibited a mixed mode of fracture along the lamellae and fracture through the lamellae, and the fracture was relatively flat. The propagated planes of the cracks that formed along the lamellae are shown in areas A and B in Fig. 13(a), and the propagated planes were relatively flat. The neat cross-section formed by the lamellar fracture is shown by the area in the white square in Fig. 13(a). Slender secondary cracks formed between the crystal lamellar colonies, as shown by the white arrows in the figure. Steps were generated in a local area, as shown in Fig. 13(b), which is similar to the morphology in Fig. 11(c), and the material fractured on multiple planes. A similar result was observed in other documents [22].

Fig. 13(c)-13(d) show the microstructure after fracture at 900 °C. The fracture surface was characterized by brittle fracture at 900 °C. However, due to the high stress, the lamellar colonies underwent severe deformation and rotation. Large tear cracks were produced, as shown in the area in the white square in Fig. 13(c). The fracture surface was relatively rough, which indicates the presence of substantial deformation.

Fig. 14 shows the microstructure of the fracture surface of the alloy after tensile fracture at 920 °C. The alloy experienced a significant high-temperature softening effect, the extent of deformation sharply increased, and there were many equiaxed dimples and pores on the fracture surface, which indicates ductile fracture, as shown in Fig. 14(a). Dissociated areas remained along the lamellae in local areas, and there

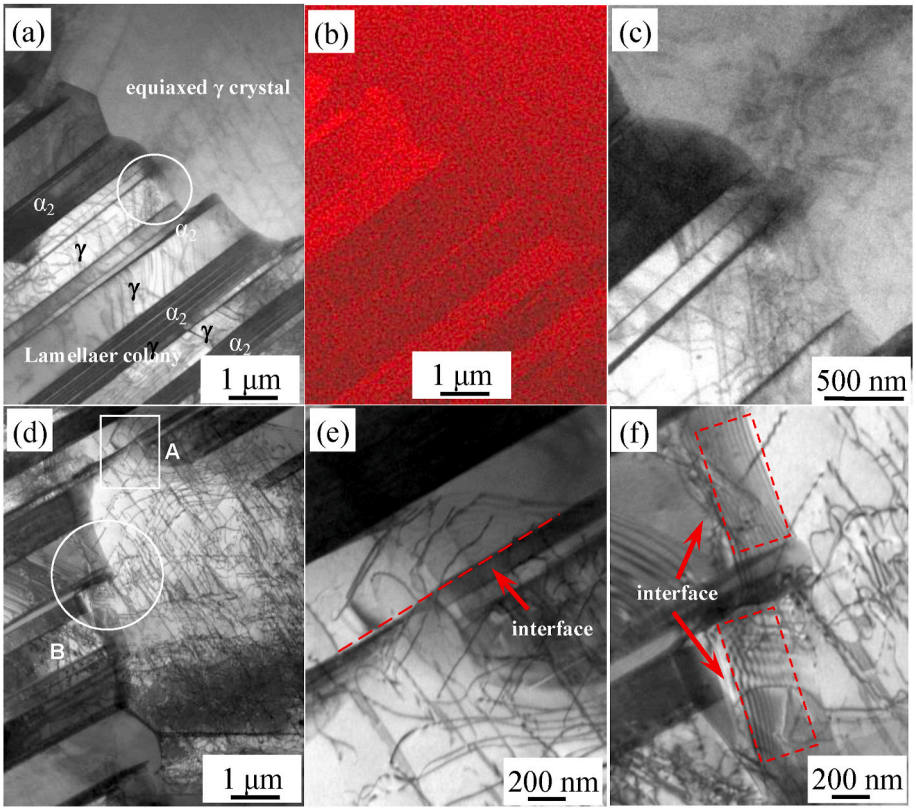

Fig. 9. Deformation features of the alloy after tensile fracture at 900 °C. (a) TEM image of the fracture microstructure; (b) EDS map of Ti; (c) enlarged view of Fig. 9 (a); (d) TEM image of the fracture microstructure; (e) enlarged view of area A in Fig. 9(d); and (f) enlarged view of area B in Fig. 9(d).

were large cracks in the boundary area of intergranular fracture and transgranular fracture, as shown in Fig. 14(b). Under this condition, micropores first formed at the material interface under the action of stress. The increase in stress caused the micropores to gradually expand to form cavities, and the cavities finally connected to form cracks, which is consistent with the microstructure in Fig. 12.

4. Discussion

The microstructure of the alloy was composed of lamellar colonies and coarsening γ phase (lamellar colony boundaries), and the lamellar colonies were composed of γ lamellae and α_2 lamellae. The deformation occurred mainly in the γ phase due to the strength of γ-TiAl phases is weaker compared to the α_2 phase. As the temperature increases, the alloy deformation falls into three stages, namely the brittle stage, the transitory stage and the ductile stage.

During the brittle stage of the TiAl–Nb alloy, the deformation of the alloy is mainly controlled by twins and dislocations. At lower temperatures, deformation preferentially occurs in the coarsening γ phase between the lamellar colonies, since the γ lamellae was limited by the α_2 lamellae near it. The dislocations could not cross the interface between the lamellar colony and coarsening γ phase and piled up on the interface, as shown in Fig. 6. With an increase in temperature, dislocation and dislocation arrays bowed out from the phase interface and twins were emitted from the γ/γ interface, twins and dislocations could be produced individually or together. In addition, γ/γ phase boundaries absorbed the lattice dislocation, enhance the diffusion in the boundaries and result in a concentration of active dislocation sources, as shown in Fig. 7. This result indicates that significant constrained stresses can develop due to the different deformation characteristics of the γ lamellae and α_2 lamellae. Twins, dislocations and dislocation arrays generated at the interfaces may effectively contribute to the accumulation of stress concentrations. The interface mechanisms support dislocation generation and improve the ductility and damage tolerance of the TiAl alloy.

In this stage, as the dislocation density rose, the driving force of the processing hardening increased and the DRV began and gradually strengthened. As seen by the slope of the tensile curve, the rate of DRV increased as the temperature increased. Despite this, the DRV worked far less than processing hardening. In addition, less slip systems can be activated, and the dislocation density increases sharply during working hardening stage, the alloy fracture in a short time. In this stage, there was not enough time to produce DRX.

During the transitory stage, with an increase in temperature and strain, the dislocation density increased, and a small number of dislocations may have passed through the interface from the coarsening γ phase into the γ lamellae, as shown in Fig. 6 and 9.

During the ductile stage of the TiAl–Nb alloy, DRX became the dominant process. The dislocations in the γ lamellae rearranged at high temperature and formed dislocation network, as shown in Fig. 10(a). As the strain strongly increased, the dislocations interacted with the dislocation network and formed subgrain boundaries, which may be the reason that more LAGBs appeared in the γ lamellae, and DRV occurred in this process, as shown in Figs. 5(c) and figure 10(c). The orientation relationship of the subgrains generates small angular shifts, as shown by the green grains and light green grains in Fig. 5(e), and the γ lamellae transformed into smaller grains through DRX, as shown in Fig. 5(e) and Figure 10(e), which indicates that DRX occurred and may be the reason that HAGBs appeared in the subgrains [23]. The γ/γ interfaces disappeared, and some broken α_2 lamellae dissolved, coarsening the γ lamellae, as shown in Figs. 3(b), Fig. 5 (b) and Fig. 10 (d). This may increasing the volume fraction of the γ phase, which increased the plasticity of the alloy. The orientation relationship of the γ lamellae became more complex, indicating that the γ lamellae rotated after high-temperature tensile testing, as shown in Fig. 3(e) and Figure 5(e). The dislocation density decreased due to the dislocation walls and diffusion processes, as shown in Fig. 10(b)-10(c).

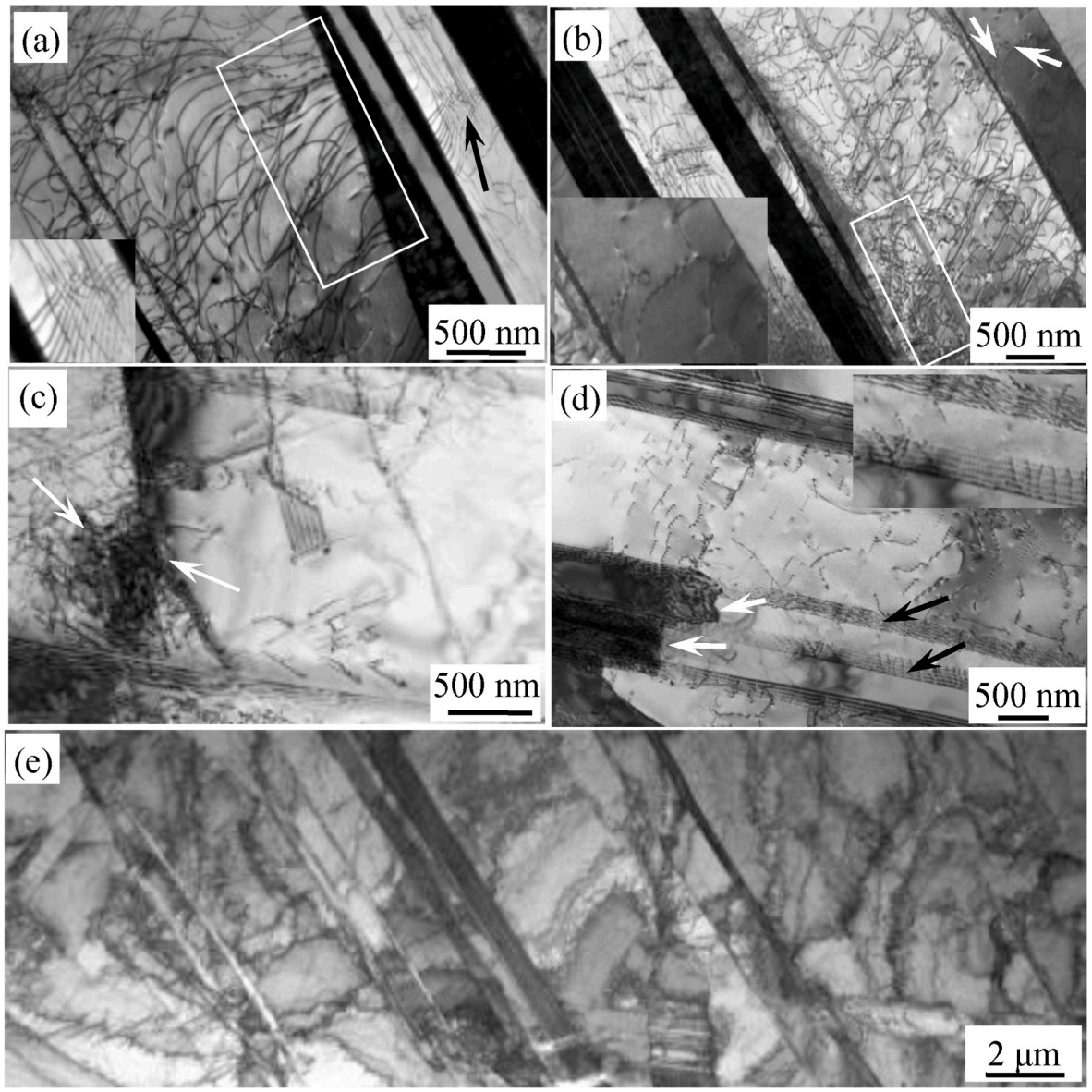

Fig. 10. Deformation features in the ductile phase of the alloy until fracture: (a) dislocation perpendicular to the γ/α_2 interface; (b) dislocation wall; (c) sub-boundary; (d) dissolved α_2 phase; and (e) dynamically recrystallized grains.

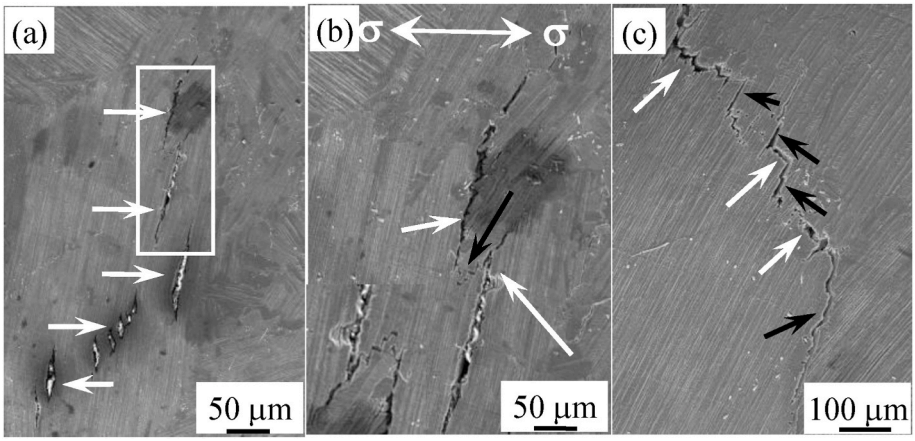

Fig. 11. Initiation and propagation of cracks in the alloy from 820 °C –840 °C: (a)–(b) 820 °C and (c) 840 °C.

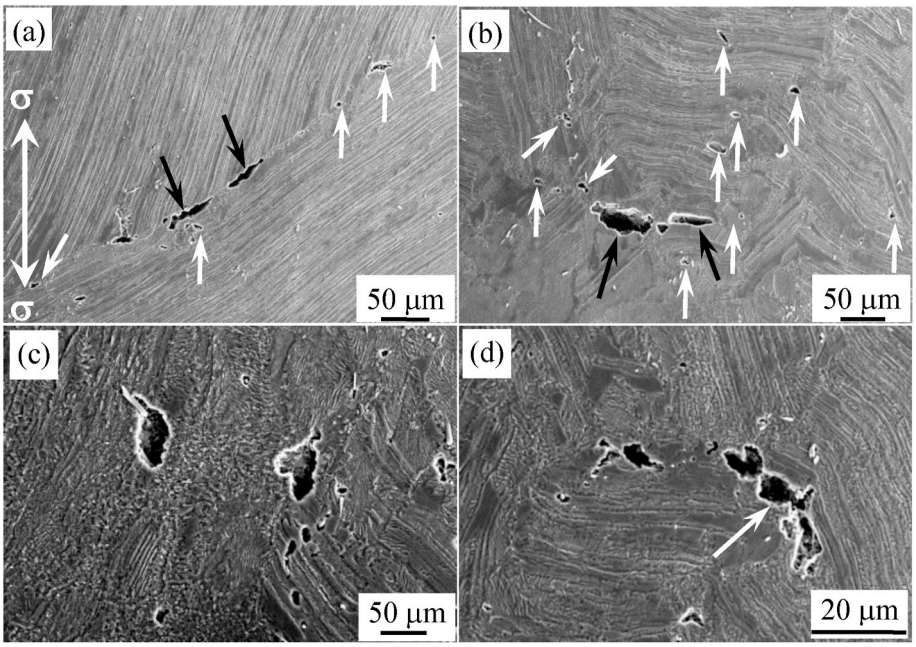

Fig. 12. Deformation features of the alloy in tension until fracture at 920 °C: (a)–(b) cracks expanding in the lamellar colony boundary and (c)–(d) cracks expanding in the DRX region.

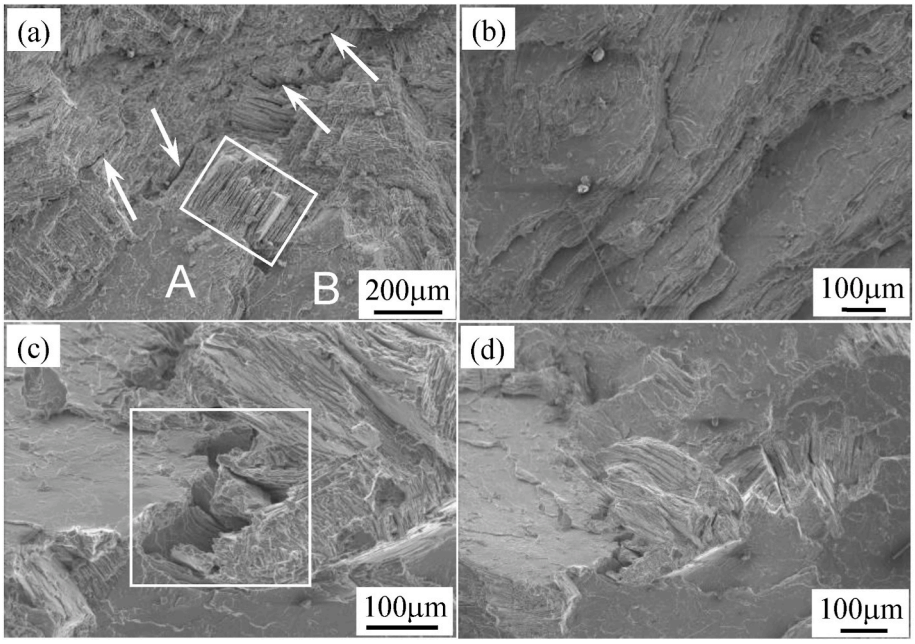

Fig. 13. Microstructure after tensile rupture at 800 °C–900 °C: (a)–(b) 800 °C and (c)–(d) 900 °C.

In this stage, the curves with a peak and then decreased, this indicate recovery and recrystallization occurred in the sample. Under these conditions, the thermal activation is enhanced, the mobility of dislocations and the slip system increased. With the increase of temperature, the critical dislocation density decreased, the critical strain of DRX is smaller and the peak stress caused by work hardening reduced. Research has shown that the critical strain for the occurrence of DRX has been found at around 0.5–0.7 times of peak strain [24]. Accordingly, the initiation of DRX for alloy would become earlier with increasing temperature and led to the increase of the fraction of recrystallized grains. This is consistent with the microstructure observed above, and similar results have been observed in other references [24]. The dislocations interacted with the dislocations to form subboundaries and promoted DRX, which is the main reason that the alloy transformed from brittle to ductile. The critical tangent stress required to activate twinning is much higher than the dislocation slip, so no twins were found in the ductile stage.

The crack propagation path is closely related to the angle between the lamellar direction and stress axis direction. During the brittle stage, cracks mainly travelled within the lamellar colonies. The cracks could spread between two adjacent lamellar colonies by smooth edges or tearing edges, as shown in Fig. 11(b). When the angle between the lamellar direction and stress axis direction was small, step-like cracks formed. During the ductile stage, DRX occurred. cavities could be

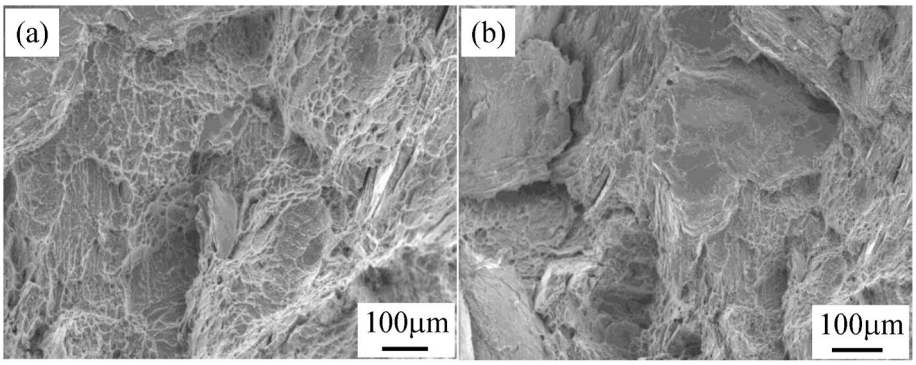

Fig. 14. Microstructure after tensile rupture at different temperatures: (a) equiaxed dimples and pores and (b) solution-treated alloy.

generated in the lamellar colony boundary and lamellar colony but only expanded in the lamellar colony boundary.

5. Conclusion

1) The brittle-ductile transition temperature of the TiAl–Nb alloy is 880–920 °C, and the alloy tends to be ductile at 900 °C.
2) During the tensile process, deformation first mainly occurs in the coarsening γ phase; when the strain increases, deformation occurs in the coarsening γ phase and γ lamellae. The contribution of α_2 to deformation is small.
3) The deformation of the alloy in the brittle stage is mainly controlled by the interaction of the twins, dislocations, γ/γ interface and γ/α_2 interface.
4) The deformation of the alloy in the ductile stage is controlled by the dislocations and phase transformation. The phase transformation, proliferation of dislocations, DRV and DRX are the main reasons for the decrease in alloy strength and increase in plasticity.
5) With increasing temperature, the fracture mode of the alloy changes from a mixed fracture mode of transgranular fracture and translaminar fracture to intergranular fracture.

CRediT authorship contribution statement

Shunke Zhang: Writing – review & editing, experiment. **Ning Tian:** Conceptualization. **Deyuan Li:** Conceptualization, Data curation, Writing – original draft. **Jianghua Li:** Data curation, Writing – original draft. **Fangwei Jin:** Data curation, Writing – original draft. **Guangyan Wang:** Data curation, Writing – original draft. **Sugui Tian:** Data curation, Writing – original draft.

Declaration of competing interest

The authors declare that they have no known competing financial interests or personal relationships that could have appeared to influence the work reported in this paper.

Acknowledgements

This work was supported by the Young Science and Technology Talent Development Project of the Education Department of Guizhou Province (KY[2019]163), Science and Technology Foundation Project of Guizhou Province (qiankehejichu [2020]1Y198, qiankehezhicheng [2019]2870), Science and Technology Project of Bijie City (bikehezi [2019]2), Characteristic Key Laboratory of University of Guizhou Province (qianjiaoheKYzi[2019]053, Coal & Phosphorus Chemical Engineering Technology Center of Bijie City ([2015]1) and Science and Technology Project of Bijie City (bikehezi[2017]05).

References

[1] Y.W. Kim, S.L. Kim, Advances in gammalloy materials–presses–application technology: successes, dilemmas, and future, J. Occup. Med. 70 (4) (2018) 553–560.
[2] L. Cha, H. Clemens, G. Dehm, Microstructure evolution and mechanical properties of an intermetallic Ti-43.5Al-4Nb-1Mo-0.1B alloy after aging below the eutectoid temperature, Int. J. Math. Res. 102 (2011) 703–708.
[3] T. Leitner, M. Schloffer, S. Mayer, J. Eßlingerc, H. Clemens, R. Pippan, Fracture and R-curve behavior of an intermetallic b-stabilized TiAl alloy with different nearly lamellar microstructures, Intermetallics 53 (2014) 1–9.
[4] T. Voisin, J.P. Monchoux, M. thomas, C. Deshayes, A. Couret, Mechanical properties of the TiAl IRIS alloy, Metall. Mater. Trans. 47A (2016) 6097–6108.
[5] W.Y. Zhao, Y.L. Pei, D.H. Zhang, Y. Ma, S.K. Gong, H.B. Xu, The microstructure and tensile property degradation of a gamma-TiAl alloy during isothermal and cyclic high temperature exposures, Intermetallics 19 (3) (2011) 429–432.
[6] V.M. Imayev, R.M. Imayev, G.A. Salishchev, On two stages of brittle-to-ductile transition in TiAl intermetallic, Intermetallics 8 (1) (2000) 1–6.
[7] Q. Wang, R.R. Chen, D.Z. Chen, Y.Q. Su, H.S. Ding, J.J. Guo, H.Z. Fu, The characteristics and mechanisms of creep brittle-ductile transition in TiAl alloys, Mater. Sci. Eng. 767 (2019) 138393.
[8] Y.M. Tan, H.Z. Fang, R.R. Chen, Y.G. Liu, Y.Q. Su, J.J. Guo, H.Z. Cui, S.Y. Zhang, H. Z. Fu, Microalloying effects of Ho on microstructure evolution and high temperature properties of Ti46Al4Nb1Mo alloy, Intermetallics 126 (2020) 106883.
[9] Z.C. Liu, J.P. Lin, S.J. Li, G.L. Chen, Effects of Nb and Al on the microstructures and mechanical properties of high Nb containing TiAl base alloys, Intermetallics 10 (2002) 653–659.
[10] H.Z. Niu, Y.Y. Chen, S.L. Xiao, F.T. Kong, C.J. Zhang, High temperature deformation behaviors of Ti-45Al-2Nb-1.5V-1Mo-Y alloy, Intermetallics 19 (12) (2015) 1767–1774.
[11] H.W. Liu, Z.X. Li, F. Gao, Y.G. Liu, Q.F. Wang, High tensile ductility and strength in the Ti-42Al-6V-1Cr alloy, J. Alloys Compd. 698 (25) (2017) 898–905.
[12] S.H. Chen, G.A. Schumacher, Comparative sdudy of deformation structures in primary equiaxed γ-grains and γ laths of a creep deformed TiAl-based alloy, Rare Met. Mater. Eng. (2007) 454–458, 03.
[13] Y.W. Kim, S.L. Kim, Effects of microstructure and C and Si additions on elevated temperature creep and fatigue of gamma TiAl alloys, Intermetallics 53 (2014) 92–101.
[14] H.T. Jiang, S.W. Tian, W.Q. Guo, G.H. Zhang, S.W. Zeng, Hot deformation behavior and deformation mechanism of two TiAl-Mo alloys during hot compression, Mater. Sci. Eng. 719 (14) (2018) 104–111.
[15] S. Bystrzanowski, A. Bartels, A. Stark, R. Gerling, F.P. Schimansky, H. Clemens, Evolution of microstructure and texture in Ti-46Al-9Nb sheet material during tensile flow at elevated temperatures, Intermetallics 18 (5) (2018) 1046–1055.
[16] Y.D. Chu, J.S. Li, F.T. Zhao, B. Tang, H.C. Kou, Characterization of the elevated temperature compressive deformation behavior of high Nb containing TiAl alloys with two microstructures, Mater. Sci. Eng. 725 (2018) 466–478.

[17] S.K. Zhang, S.G. Tian, X. X Lv, H.C. Yu, N. Tian, Z.H. Jiao, G.Q. Zhao, D.Y. Li, Deformation and damage behaviors of as-cast TiAl-Nb alloy during creep, Prog. Nat. Sci.: Materials International 38 (2018) 618–625.
[18] W.Y. Zhao, Y.L. Pei, D.H. Zhang, Y. Ma, S.K. Gong, H.B. Xu, The microstructure and tensile property degradation of a gamma-TiAl alloy during isothermal and cyclic high temperature exposures, Intermetallics 19 (2011) 429–432.
[19] H.T. Huang, H.S. Ding, X.S. Xu, R.R. Chen, J.J. Guo, H.Z. Fu, Phase transformation and microstructure evolution of a beta-solidified gamma-TiAl alloy, J. Alloys Compd. 860 (15) (2021) 158082.
[20] G. Zlateva, Microstructure of Metals and Alloys, 2008, pp. 21–22.
[21] L. Yu, X.P. Song, M. Zhang, Z.H. Jiao, H.C. Yu, High-temperature fracture toughness of high Nb-containing TiAl alloys, Chin. J. Eng. 38 (2016) 379–384.
[22] X. Zan, Y.H. He, Y. Wang, Y.M. Xia, Dynamic behavior and fracture mode of TiAl intermetallics with different microstructures at elevated temperatures, T. Nonferr. Meta.l Soc. 21 (2011) 45–51.
[23] L. Xin, W. Wei, H. Hui, X. Liu, Z. Nie, Microstructure and mechanical properties of hot-rolled 5E83 alloy, High Performance Structural Materials (2018) 69–77.
[24] Y. Wang, W.Z. Shao, L. Zhen, L. Yang, X.M. Zhang, Flow behavior and microstructures of superalloy 718 during high temperature deformation, Mater. Sci. Eng. 497 (2008) 479–486.